Probing optimal reaction energy for synthesis of element 119 from ^{51}V+^{248}Cm reaction with quasielastic barrier distribution measurement

M. Tanaka,[1,2,3,*] P. Brionnet,[3] M. Du,[4] J. Ezold,[4] K. Felker,[4] B. J.P. Gall,[5] S. Go,[1,2,3] R. Grzywacz,[6,7] H. Haba,[3] K. Hagino,[8] S. Hogle,[4] S. Ishizawa,[3,9] D. Kaji,[3] S. Kimura,[3] T. T. King,[7] Y. Komori,[3] R. K. Lemon,[3,10] M. G. Leonard,[3,10] K. Morimoto,[3] K. Morita,[1,2,3] D. Nagae,[1,2,3] N. Naito,[3,11] T. Niwase,[1,3] B.C. Rasco,[7] J. B. Roberto,[7] K. P. Rykaczewski,[7] S. Sakaguchi,[1,2,3,†] H. Sakai,[3] Y. Shigekawa,[3] D.W. Stracener,[7] S. VanCleve,[4] Y. Wang,[3] K. Washiyama,[2] and T. Yokokita[3]

[1] *Department of Physics, Kyushu University, Fukuoka 819-0395, Japan*
[2] *Research Center for Superheavy Elements, Kyushu University, Fukuoka 819-0395, Japan*
[3] *RIKEN Nishina Center for Accelerator-Based Science, Wako, Saitama 351-0198, Japan*
[4] *Oak Ridge National Laboratory, Oak Ridge, Tennessee 37831, USA*
[5] *Université de Strasbourg, CNRS, IPHC UMR 7178, 67037 Strasbourg, France*
[6] *Department of Physics and Astronomy, University of Tennessee, Knoxville, Tennessee 37996, USA*
[7] *Physics Division, Oak Ridge National Laboratory, Oak Ridge, Tennessee 37831, USA*
[8] *Department of Physics, Kyoto University, Kyoto 606-8502, Japan*
[9] *Graduate School of Science and Engineering, Yamagata University, Yamagata 990-8560, Japan*
[10] *Department of Nuclear Physics and Accelerator Applications,*
Research School of Physics, The Australian National University,
Canberra, Australian Capital Territory 2601, Australia
[11] *Graduate School for Science, Kyushu University, Fukuoka 819-0395, Japan*

(Dated: May 25, 2022)

The quasielastic barrier distribution of ^{51}V+^{248}Cm was extracted by measuring the excitation function of quasielastic backscattering using a gas-filled recoil ion separator, GARIS-Ⅲ. The obtained barrier distribution is well explained by the coupled-channels calculation, indicating a significant effect of the rotational excitation of deformed ^{248}Cm. From the measured average Coulomb barrier height and deformation parameters of ^{248}Cm, the side-collision energy leading to a compact configuration of colliding nuclei was obtained. The relation between the side collision energy and the excitation function of the evaporation-residue cross sections in the ^{48}Ca+^{248}Cm system was evaluated as a reference for the ^{51}V+^{248}Cm case. The optimal reaction energy to synthesize a new element 119 at the ^{51}V+^{248}Cm fusion reaction (3n and 4n channels) was estimated with an aid of these experimental data.

I. INTRODUCTION

With the official recognition of superheavy elements (SHEs) with atomic numbers $Z = 113, 115, 117$, and 118 in 2016, the periodic table is now completely filled up to the seventh period. The discovery of new elements in the SHE region and their nuclear properties provide essential information about the limits of nuclear existence and the island of stability expected to exist in the $Z = 114$ or 120 and $N = 184$ regions [1].

The elements beyond $Z = 113$ were synthesized only by hot-fusion reactions using a combination of ^{48}Ca beams and targets of actinide elements from Pu ($Z = 94$) to Cf ($Z = 98$) [2–7]. However, because it is impossible now to obtain the elements heavier than Cf at the amounts needed for the target material, it is necessary to use projectiles heavier than ^{48}Ca to synthesize new elements beyond $Z = 118$. Although the synthesis of elements 119 and 120 has been attempted in several cases via $^{244}\mathrm{Pu}(^{58}\mathrm{Fe}, xn)^{302-x}120$, $^{238}\mathrm{U}(^{64}\mathrm{Ni}, xn)^{302-x}120$, $^{248}\mathrm{Cm}(^{54}\mathrm{Cr}, xn)^{302-x}120$, $^{249}\mathrm{Bk}(^{50}\mathrm{Ti}, xn)^{299-x}119$, and $^{249}\mathrm{Cf}(^{50}\mathrm{Ti}, xn)^{299-x}120$, these new elements have not been discovered yet [8–11].

In the synthesis of SHEs using the fusion-evaporation reaction, the beam energy is a critical parameter that significantly affects the experimental yield of heaviest elements. For example, the evaporation residue (ER) cross section σ_{ER} of $^{248}\mathrm{Cm}(^{48}\mathrm{Ca}, 4\mathrm{n})^{292}\mathrm{Lv}$ is $3.4^{+2.7}_{-1.6}$ pb at $E_{\mathrm{c.m.}} = 208.9$ MeV [5, 12], whereas the experimental upper limit of this cross section is 0.3 pb at $E_{\mathrm{c.m.}} = 201.0$ MeV at [5]. Thus, an energy difference of just 7.9 MeV (3.8%) can change the cross section by approximately one order of magnitude. The energy of the projectile nucleus decreases as it passes through a target. Typically, the energy change of the projectile nucleus in the target used in these experiments is less than ±3 MeV relative to the energy at the center of the target, which is narrower than the width of the excitation function of σ_{ER}. In the case of a reaction, where σ_{ER} has never been measured, the theoretical prediction of the optimal reaction energy for maximizing σ_{ER} can vary by more than 10 MeV depending on the theoretical model adopted. For example, in the $^{248}\mathrm{Cm}(^{51}\mathrm{V}, xn)^{299-x}119$ reaction focused in this study, the theoretical optimal energy varies from 230 MeV to 246 MeV in the center-

---

[*] masaomi@phys.kyushu-u.ac.jp
[†] sakaguchi@phys.kyushu-u.ac.jp

of-mass system [13–17]. The cross sections predicted by these theoretical calculations are well below 100 fb, which are much smaller than those in the previous ER synthesis by hot fusion reactions. Therefore, to synthesize the element 119 with the maximum efficiency using the $^{248}\mathrm{Cm}(^{51}\mathrm{V}, xn)^{299-x}119$ reaction, it is desirable to estimate the incident energy based on experimental evidence.

The barrier distribution extracted from the excitation function of the quasielastic (QE) cross section relative to the Rutherford cross section [18, 19] is expected to be one of the most powerful methods for experimentally estimating the optimal incident energy to maximize σ_{ER}. The QE barrier distribution reflects the reaction dynamics of the two colliding nuclei during the capture process, which is the first step in the ER nucleus formation. The relation between the QE barrier distribution and σ_{ER} has been systematically studied in reaction systems that form superheavy nuclei (SHN) [20–25]. In cold fusion systems, the peak energy of the QE barrier distribution and the optimal energy to maximize σ_{ER} are consistent [20, 23, 24]. However, Tanaka *et al.* recently pointed out that the optimal energy for σ_{ER} is slightly higher than the peak of the QE barrier distribution in hot-fusion reaction [25]. It has also been reported from fusion-fission studies that, in a reaction system with an actinide target, a compound nucleus is formed more easily when the colliding nuclei touch each other along the short axis of the prolately-deformed target nucleus, which is called a side collision [26–31]. This is considered to be a consequence of the compact configuration of the colliding nuclei at the touching point. In hot-fusion reaction systems where the experimental data of both σ_{ER} and QE barrier distribution were available, the energy for the side collision derived from the QE barrier distribution data was in good agreement with the experimental optimal energy of σ_{ER} [25]. This study points out that the optimal energy can be experimentally estimated by measuring the QE barrier distribution in a reaction system in which ER production has not yet been performed.

The systematic measurements of the QE barrier distribution mentioned above have been performed at the RIKEN heavy-ion linear accelerator (RILAC) facility using the gas-filled recoil ion separator GARIS [23–25]. However, the QE barrier distribution has not been measured for the system forming a nucleus with $Z = 119$ because a sufficiently high incident energy to measure the complete dataset of the QE barrier distribution could not be supplied in this facility. Recently, the RILAC facility was upgraded for synthesizing new elements beyond $Z = 118$ [32]. The upgraded facility, called SRILAC, can accelerate heavy ions up to 6.5 MeV/nucleon by replacing the last four normal conducting cavities in the RILAC booster with ten superconducting cavities [32]. This upgrade enabled us to measure the QE barrier distribution of the hot-fusion-reaction system, forming an element with $Z \geq 119$.

In this study, we report the first experimental study of the QE barrier distribution of $^{51}\mathrm{V}+^{248}\mathrm{Cm}$, which is the target reaction for synthesizing the element 119 at RIKEN, by measuring the excitation function of the QE backscattering cross section relative to the Rutherford cross section. The obtained barrier distribution was compared with the coupled-channels calculations to understand the reaction dynamics. The energy for the side collision that leads to a compact touching configuration favorable for the formation of the ER nucleus was deduced. The relation between the side-collision energy and the optimal reaction energy to maximize the ER cross section was investigated based on the existing experimental data of the system similar to $^{51}\mathrm{V}+^{248}\mathrm{Cm}$. Finally, the optimal reaction energy for synthesizing the element 119 from the $^{51}\mathrm{V}+^{248}\mathrm{Cm}$ fusion reaction was deduced based on the present experimental results.

II. EXPERIMENT AND ANALYSIS

A. Experimental method

The QE barrier distribution in the $^{51}\mathrm{V}+^{248}\mathrm{Cm}$ system was extracted by measuring the QE backscattering. Unlike typical measurements that detect the QE scattering of a projectile-like nucleus at backward angles [18, 19], in this study, the measurement was performed by detecting the QE scattering of the recoiled target-like nucleus at 0°, which corresponds to the backscattering of the incident nucleus at 180° [23–25]. This method allows us to directly measure the reaction with angular momentum $l \sim 0$, which is the most important component in the production of the ER nucleus.

The barrier distribution $D(E)$ via QE backscattering is obtained by the following equation:

$$D(E) = -\frac{dR}{dE} \equiv -\frac{d}{dE}\left(\frac{d\sigma_{\mathrm{QE}}}{d\sigma_{\mathrm{Ruth}}}\right), \tag{1}$$

¡ where $R \equiv d\sigma_{\mathrm{QE}}/d\sigma_{\mathrm{Ruth}}$ is the ratio of the cross section of QE backscattering to that of Rutherford scattering at a fixed angle and is called the reflection probability. The $R(E)$ value was extracted by measuring the number of recoiled QE events of the $^{248}\mathrm{Cm}$-like nucleus at $\theta_{\mathrm{Lab}} = 180°$, $N_{\mathrm{QE}}[^{248}\mathrm{Cm}]$, and the number of Rutherford scattering events of the projectile $^{51}\mathrm{V}$ at $\theta_{\mathrm{Lab}} = 45°$, $N_{\mathrm{Ruth}}[^{51}\mathrm{V}]$:

$$\begin{aligned} R &= \frac{(d\sigma_{\mathrm{QE}})_{180°}}{(d\sigma_{\mathrm{Ruth}})_{180°}} \\ &= \frac{(d\sigma_{\mathrm{QE}})_{180°}}{(d\sigma_{\mathrm{Ruth}})_{45°}} \cdot \frac{(d\sigma_{\mathrm{Ruth}}/d\Omega)_{45°}}{(d\sigma_{\mathrm{Ruth}}/d\Omega)_{180°}} \\ &= \frac{N_{\mathrm{QE}}[^{248}\mathrm{Cm}]}{N_{\mathrm{Ruth}}[^{51}\mathrm{V}]} \cdot \left[\frac{\Delta\Omega_{\mathrm{QE}}[^{248}\mathrm{Cm}]}{\Delta\Omega_{\mathrm{Ruth}}[^{51}\mathrm{V}]}\right]^{-1} \cdot \frac{(d\sigma_{\mathrm{Ruth}}/d\Omega)_{45°}}{(d\sigma_{\mathrm{Ruth}}/d\Omega)_{180°}} \\ &\equiv C \cdot \frac{N_{\mathrm{QE}}[^{248}\mathrm{Cm}]}{N_{\mathrm{Ruth}}[^{51}\mathrm{V}]}. \end{aligned} \tag{2}$$

Here, the solid angles of the detector to count $N_{\mathrm{QE}}[^{248}\mathrm{Cm}]$ and $N_{\mathrm{QE}}[^{51}\mathrm{V}]$, $\Delta\Omega_{\mathrm{QE}}[^{248}\mathrm{Cm}]$ and $\Delta\Omega_{\mathrm{Ruth}}[^{51}\mathrm{V}]$, are fixed values, and the ratio of the Rutherford scattering cross section at $\theta_{\mathrm{Lab}} = 45°$ and $\theta_{\mathrm{Lab}} = 180°$, $(d\sigma_{\mathrm{Ruth}}/d\Omega)_{45°} / (d\sigma_{\mathrm{Ruth}}/d\Omega)_{180°}$, is constant and independent of the reaction energy. In Eq. (2), the product of the constant parts is defined as C. In this experiment, the grazing angle at the maximum center-of-mass energy, $E_{\mathrm{c.m.}} = 247.1$ MeV, was $\theta_{\mathrm{Lab}} = 106°$ in the laboratory system. Therefore, the angle to count $N_{\mathrm{Ruth}}[^{51}\mathrm{V}]$, $\theta_{\mathrm{Lab}} = 45°$, satisfies the condition of always monitoring the Rutherford scattering at all measurement energies.

B. Experiment

The experiment was performed at the superconducting RIKEN heavy ion linear accelerator) facility (SRILAC) [32]. The $^{51}\mathrm{V}^{13+}$ ions were extracted from a 28 GHz superconducting ECR ion source and injected into the SRILAC. The typical beam intensity in this study was approximately 25 pnA, corresponding to 1.6×10^{11} particles per second. The measurements were performed at incident energies in 247.3–324.4 MeV with 2.0 MeV steps. The corresponding energy range at the center of the target in the center-of-mass system, $E_{\mathrm{c.m.}}$, was between 182.1 MeV and 247.1 MeV. The incident beam energies were determined by measuring the magnetic rigidity in a 90°-bending dipole magnet and the time-of-flight (TOF). The accuracy of the beam energy measurement by these methods is typically less than 0.1%, excluding systematic uncertainties [32, 53].

The $\mathrm{Cm_2O_3}$ target with a thickness of 483(15) μg/cm^2 was used. The high-weight percent ^{248}Cm was harvested from recently decayed ^{252}Cf material provided by the U.S. Department of Energy's Isotope Program, ^{252}Cf Production Program at ORNL. Following the initial separation using a cation-exchange column, in various molarities and pH values of an alpha-hydroxy-isobutyrate (AHIB) solution, the curium was further processed through diglycolamide (DGA) and LN (di(2-ethylhexyl) orthophosphoric acid (HDEHP)) resin columns. The DGA resin was employed to separate the curium from fission products and decay daughters of ^{252}Cf. The LN separated the curium from remaining ^{252}Cf. The curium stock was provided as a dried nitrate salt. The isotopic composition of the Cm target was 96.96% ^{248}Cm, 0.01% ^{247}Cm, 3.00% ^{246}Cm, and 0.03% ^{245}Cm. The $\mathrm{Cm_2O_3}$ material was electrodeposited on a Ti backing with a thickness of 1.31 mg/cm^2, and oriented to the downstream side. The target was used in a fixed position because there was no risk of melting under low beam intensity in this experiment. The typical size of the beam spot on the target was 3 mm (H)× 10 mm (V).

The recoiled events of the target-like nuclides at 0° by QE backscattering were separated from the background events and transported to the final focal plane by using the gas-filled recoil ion separator GARIS-III. GARIS-III was newly constructed at the SRILAC facility and has the same specifications as GARIS-II [34]. The GARIS-III was filled with 0.9-Torr He gas, and the vacuum of the upstream beamline was maintained at a sufficiently high level by the differential pumping system. The vacuum chamber at the final focal plane was isolated from GARIS-III using a 0.5-μm Mylar foil to secure a high-vacuum condition for the operation of the detectors. The magnetic rigidity of GARIS-III, $B\rho$, was carefully set such that the transmission efficiency of recoiled target-like events to the final focal plane was maintained above 95% of its maximum value. As will be described in Sec. II C, the relative transmission efficiency was measured and corrected in the data analysis. The $B\rho$ values were 1.757 Tm, 1.728 Tm, and 1.714 Tm for incident energies of $E_{\mathrm{c.m.}}$ =182.1–209.5 MeV, 211.1–235.2 MeV, and 236.9–247.1 MeV, respectively. The projectile particles scattered around 0° were stopped by a water-cooled tantalum beam dump located in the D1 magnet of the GARIS-III.

The recoiled target-like events were identified and counted using a TOF–E counter telescope placed at the final focal plane, where E represents the total energy. The TOF was measured by two electrostatic TOF detectors consisting of an entrance foil, an electrostatic mirror, and a microchannel plate (PHOTONIS 120-D-40:1-NR) [35]. The entrance foil was a 0.5-μm-thick Mylar foil with 19.3 μg/cm^2 (100$\mathring{A}$) gold deposited on it. The distance between the two TOF detectors was 273 mm. Two double-sided silicon strip detectors (DSSDs: Micron Semiconductor Ltd. BB-7) were used as the E detectors. These two DSSDs were mounted side-by-side along the momentum-dispersive direction. The E detector was divided into 32 strips (2 mm/strip) and 16 strips (4 mm/strip) along the horizontal (X: momentum dispersive direction) and vertical (Y: gravity direction) axes, respectively, to measure the position of recoiled target-like events at the focal plane. The effective areas of the TOF and E detectors are 120 mmϕ and 128 mm(H)×64 mm(V), respectively.

The number of ^{51}V events by Rutherford scattering at 45° degree, $N_{\mathrm{Ruth}}[^{51}\mathrm{V}]$, was counted using a Si detector (Hamamatsu S1223-01). The distance between the target and the Si detector was 213 mm, and the sensitive area of the Si detector was collimated to 2.5 mmϕ.

C. Data analysis

Figure 1 shows typical plots of the particle identification using the TOF–E telescope for counting recoiled target-like events at $E_{\mathrm{c.m.}} = 182.1$, 214.6, and 247.1 MeV. When particles fired two neighboring strips in the DSSD, the sum of the detected energies in both strips was treated as an E value. The correlation function between TOF and E for events with mass number $A = 248$ is indicated by red dashed lines to clarify the locus of target-

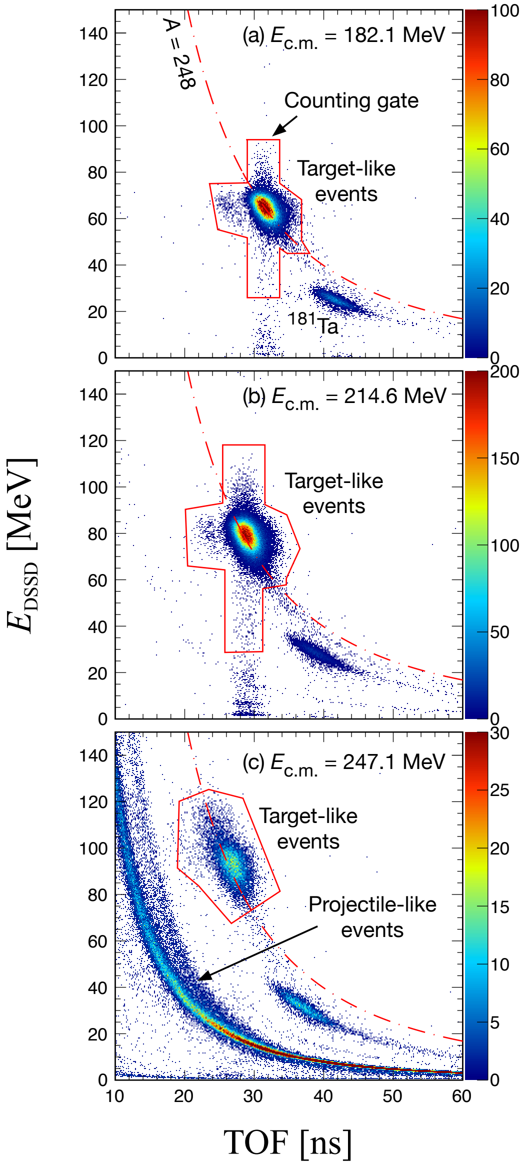

FIG. 1. Particle-identification plots by the TOF–E telescope at (a) $E_{\text{c.m.}} = 182.1$ MeV, (b) $E_{\text{c.m.}} = 214.6$ MeV, and (c) $E_{\text{c.m.}} = 247.1$ MeV. The solid line indicates the counting gate. The dashed line represents the function $A = 248$.

like events. In the calculation of the correlation function, the loss of detected energy due to the effect of the pulse-height defect in DSSD was considered [36]. The target-like events were clearly separated from the background, such as projectile-like events and ^{181}Ta, which were also identified by the same procedure as the target-like events in all measured data. The ^{181}Ta background is considered to be caused by sputtering out of ^{181}Ta from the beam dump in the D1 magnet owing to the collision of the projectile particles. These target-like events were counted as recoiled events by the QE backscattering $N_{\text{QE}}[^{248}\text{Cm}]$. Here, an arbitrarily shaped counting gate (red solid line) was adopted so that even events located outside the main peak owing to the response of the detectors and the reactions in the detectors would not be missed. The number of events located at the main peak is approximately 98% of the total number of events within the counting gate.

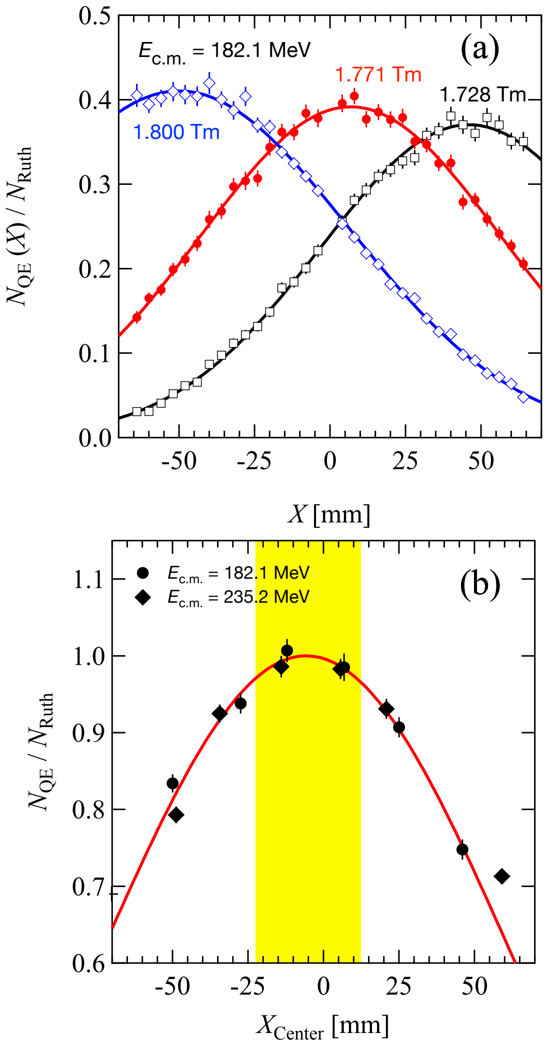

FIG. 2. (a) Horizontal (X) yield distributions of target-like events in DSSDs at $E_{\text{c.m.}} = 182.1$ MeV. The blue open squares, red closed circles, and black open diamonds indicate the data with the magnetic rigidity of 1.800, 1.711, and 1.728 Tm, respectively. The solid lines represent the fitting results obtained using the Gaussian function. (b) Relative transmission efficiency at $E_{\text{c.m.}} = 182.1$ MeV (circles) and 235.2 MeV (diamonds) as a function of the center of horizontal position X_{center}. The solid line indicates the fitting result obtained using a quadratic function. The X_{center} values of all the data used to derive the barrier distribution are located within the shaded region.

Although GARIS-III has a large acceptance, not all the target-like events caused by QE scattering are transported to the final focal plane. The full width at half maximum (FWHM) of the vertical (Y) yield distribution at the focal plane was typically 12 mm, which was well covered by the effective area along the Y axis (64 mm) of the counter telescope. However, the typical FWHM of the yield distribution in the horizontal (X) direction was approximately 80 mm, which is comparable to the effective area of the counter telescope (120 mm). In other words, the spatial relation between the yield distribution of target-like events on X and the effective area of the counter telescope has a possibly influence on the transmission efficiency. Therefore, we measured the dependence of the transmission efficiency of the QE target-like events through GARIS-Ⅲ on the magnetic rigidity of the GARIS-Ⅲ at $E_{\mathrm{c.m.}} = 182.1$ and 235.2 MeV.

Figure 2(a) shows the yield distributions of QE target-like events on X normalized by N_{Ruth}, $N_{\mathrm{QE}}(X)/N_{\mathrm{Ruth}}$, for $B\rho = 1.728$ (black open diamonds), 1.771 (red solid circles), and 1.800 Tm (blue open squares) at $E_{\mathrm{c.m.}} = 182.1$ MeV. Here, the momentum dispersion at the focal plane derived from these data was 20.8(4) mm/%, which is roughly consistent with the design value of GARIS-Ⅲ (19.7 mm/%) [34]. The center position of the distribution, X_{center}, was derived by fitting $N_{\mathrm{QE}}(X)/N_{\mathrm{Ruth}}$ to a Gaussian function. The relation between the integrated values of the distributions shown in Fig. 2(a), $N_{\mathrm{QE}}/N_{\mathrm{Ruth}}$ (referred to as the relative transmission efficiency in this study), and X_{center} are shown in Fig. 2(b). All the data taken at two different energies exhibited a similar correlation. By appropriately adjusting the applied magnetic field of GARIS-Ⅲ appropriately, the relative transmission efficiency was maintained above 0.95 in all measurements, as indicated by the yellow shaded region in Fig. 2(b). The slight loss of transmission efficiency (< 5%) from its maximum value does not influence the following discussion. However, this loss was larger than the statistical uncertainty (typically 1%) of the data. Therefore, we corrected the effect of the relative transmission efficiency using the fitting function obtained from the $|X_{\mathrm{center}}| < 50$ mm data shown by the red solid line in Fig. 2(b). The standard deviation of the data from the fitting function at $|X_{\mathrm{center}}| < 50$ mm was 1.3%. This value was treated as a systematic uncertainty owing to the correction of the transmission efficiency.

A typical yield distribution on Y, $N_{\mathrm{QE}}(Y)/N_{\mathrm{Ruth}}$, at $E_{\mathrm{c.m.}} = 182.1$ MeV is shown in Fig. 3. For all the measured energies, the distributions were well explained by the double-Gaussian function shown by the red solid line. Based on this fitting result, the relative yield change within the active area (±64 mm) on Y was maintained at an average value of 99.1%, with a standard deviation of 0.2% for all data. This deviation around the average value was much smaller than the statistical uncertainty (∼ 1%); therefore, the correction of regarding $N_{\mathrm{QE}}(Y)/N_{\mathrm{Ruth}}$ was not necessary.

At reaction energies higher than the Coulomb barrier energy in the reaction systems forming SHNs, it has been pointed out that the energy spectrum broadens because of the contamination of the deep inelastic (DI) scattering events with the QE scattering events [20–25, 36]. In the previous barrier distribution measurement using GARIS, the experimental data in the energy region where the influence of DI scattering events was pronounced were evaluated from the change in the shape of the E spectra [23–25]. Figure 4(a) shows the E spectra at $E_{\mathrm{c.m.}} = 182.1$ (black), 214.6 (blue), and 247.1 MeV (red). The spectrum at $E_{\mathrm{c.m.}} = 247.1$ MeV (red) is significantly broader than those at lower reaction energies. To quantitatively evaluate the shape change of the spectrum, the E spectra were fitted using Gaussian functions. Figure 4(b) shows the peak width divided by the peak-center value, W/E_{peak}, obtained from the fitting result as a function of $E_{\mathrm{c.m.}}$. The width increased significantly at the five data points at $E_{\mathrm{c.m.}} \geq 240.3$ MeV. In addition, the data at $E_{\mathrm{c.m.}} \geq 240.3$ MeV have a prominent tail in the higher-E region than the main peak. Therefore, as in previous studies [23–25], these five data points were treated as upper-limit values, because they may contain a non-negligible proportion of background events.

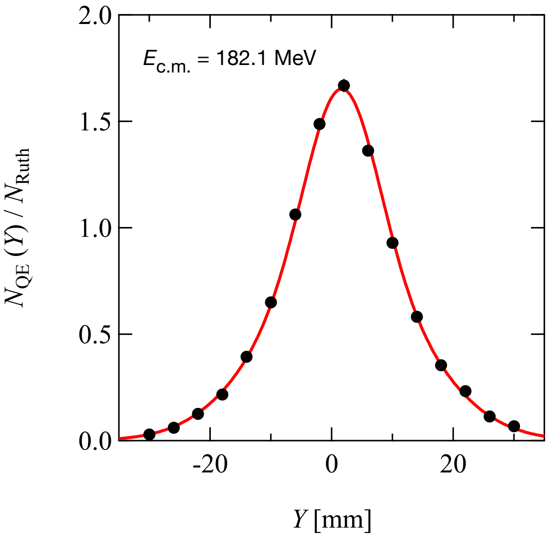

FIG. 3. (a) Vertical (Y) yield distributions of target-like events in DSSDs at $E_{\mathrm{c.m.}} = 182.1$ MeV. The solid line represents the fitting result obtained using a the double-Gaussian function. Most of the error bars are smaller than the symbol size.

D. Experimental results

The reflection probability R defined by Eq. (2), was derived from the ratio of the number of QE scattering events, $N_{\mathrm{qel}}[^{248}\mathrm{Cm}]$, counted in the above treatment to the number of Rutherford scattering events of ^{51}V, $N_{\mathrm{Ruth}}[^{51}\mathrm{V}]$. The constant part, C, in Eq. (2) was determined from 13 data points at $E_{\mathrm{c.m.}} \leq 202.6$ MeV.

The obtained excitation function $R(E)$ for ^{51}V+^{248}Cm is shown in Fig. 5(a). The data treated as upper limits

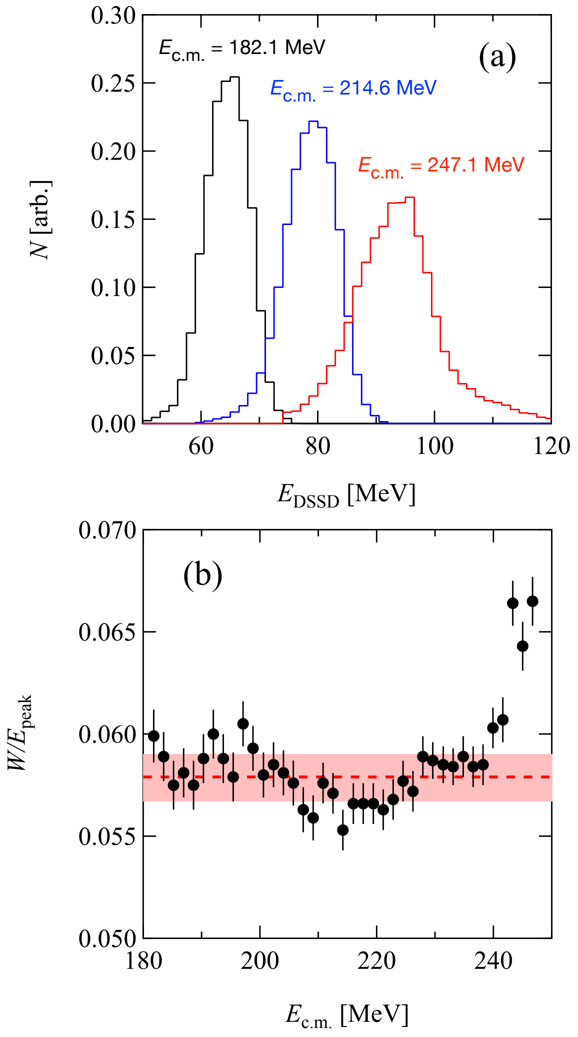

FIG. 4. (a) Energy spectra at $E_{\mathrm{c.m.}}$ = 182.1 MeV (black), 214.6 MeV (blue), and 247.1 MeV (red). (b) Values of the peak width W divided by the peak center E_{peak} of the fitting results to the energy spectra using the single-Gaussian function. The red line and shaded region indicate the average value and the standard deviation of the data at $E_{\mathrm{c.m.}} \leq$ 238.6 MeV.

owing to the contamination of some background events are represented by open circles. From the $R(E)$ data, the QE barrier distribution $D(E)$ was obtained using the following two-point difference formula (Fig. 5(b)):

$$D(E_i) = \frac{R(E_{i+1}) - R(E_{i-1})}{E_{i+1} - E_{i-1}}. \tag{3}$$

The energy step $E_{i+1} - E_{i-1}$ of the derivative is 3.4 MeV. Here, the $D(E)$ values were obtained, except for the region of $E_{\mathrm{c.m.}} > 236.9$ MeV, where the finite values of $R(E)$ at $E_{\mathrm{c.m.}} \geq 240.3$ MeV were not available.

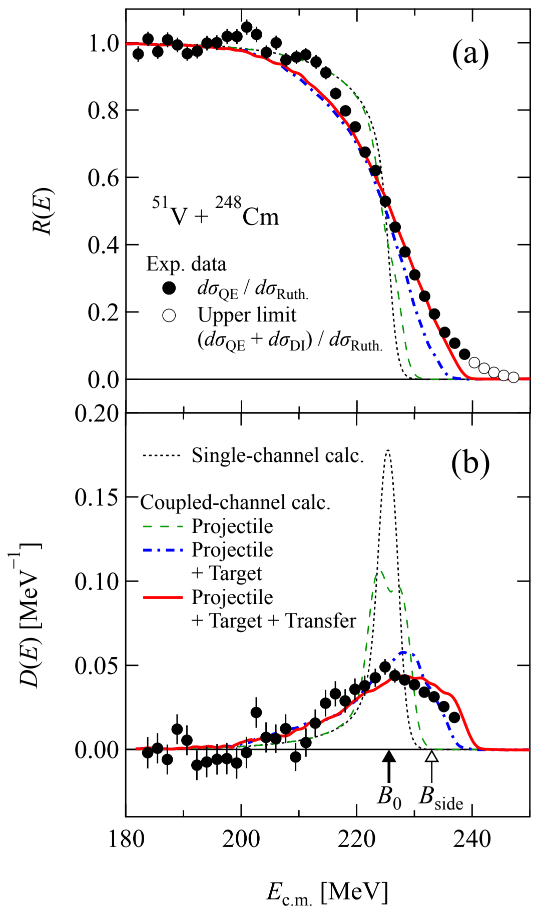

FIG. 5. (a) Excitation function of the QE backscattering cross section relative to the Rutherford cross section $R(E)$. (b) Barrier distribution derived from the experimental R values. The respective lines indicate the coupled-channels calculations (see text for details). The black closed and open arrows indicate the values of B_0 (Eq. (5)), and B_{side} (Eq. (7)).

III. DISCUSSION

A. Comparison with coupled-channels calculations

First, to understand the reaction dynamics of the ^{51}V+^{248}Cm system, we compared the present results of $R(E)$ and $D(E)$ with coupled-channels calculations using the CCFULL code [37]. In this calculation, the vibrational excitation of the projectile nucleus ^{51}V, rotational excitation of the target nucleus ^{248}Cm, and coupling of the neutron transfer reaction were considered as a fully coupled case.

The calculation parameters used are shown in Table I. For the values of the radius constant r_0 and diffuseness a_0 in the real part of the optical potential, we adopted empirical parameters [38] by Akyüz and Winther. The parameters for the imaginary part of radius constant (r_w), diffuseness (a_w), and potential depth (V_w) are the same as those in previous studies of reaction systems, similar

TABLE I. Applied parameters for the coupled-channels calculations.

Optical potential		
Real part		
$V_0 = 115$ MeV	$r_0 = 1.19$ fm	$a_0 = 0.70$ fm
Imaginary part		
$V_w = 50.0$ MeV	$r_w = 1.00$ fm	$a_w = 0.40$ fm
Excitation of ^{51}V (Quadrupole vibrational coupling)		
$\beta_2 = 0.11$	$E_{1\mathrm{ph}} = 0.320$ MeV	$N_{\mathrm{ph}} = 1$
Excitation of ^{248}Cm (Rotational coupling)		
$\beta_2 = 0.286$	$\beta_4 = 0.039$	$\beta_6 = 0.030$
Coupling of neutron-transfer reaction		
$F_{\mathrm{tr}} = 0.25$	$Q = 1.12$ MeV	

to the present one [20, 23, 25]. The quadrupole vibrational coupling was assumed as the excitation of the incident nucleus ^{51}V. The value of the excitation energy of the single-phonon state $E_{1\mathrm{ph}}$ was obtained from the existing experimental value of the first excited state [39]. The quadrupole deformation parameter β_2 was determined based on the experimental value of the reduced quadrupole transition probability $B(E2)$ [39]. In the present calculations, the finite spin of the ground state of ^{51}V was ignored, and only one phonon excitation was considered (N_{ph}=1). Note that the coupled-channels calculation of the fusion barrier distribution for ^{36}S+^{51}V is almost independent of the exact consideration of the additional one proton $1f_{7/2}$ on ^{50}Ti, which takes into account the finite spin of the ground state of ^{51}V [40]. For the excitation of the target nucleus ^{248}Cm, rotational coupling due to deformation up to the sixth order, i.e., β_2, β_4, and β_6, was considered. The effect of rotational excitation was treated based on the average formula for the orientation angle of a deformed nucleus [19, 41, 42]. In this method, the reflection probability is calculated as a function of the energy and orientation angle θ of the deformed target, $r(E, \theta)$, and the $R(E)$ value is obtained as an integral of $r(E, \theta)$ over θ:

$$R(E) = \int_0^{\pi/2} r(E, \theta) \sin\theta d\theta. \tag{4}$$

The value of β_2 was determined from the experimental value of $B(E2)$ [43]. On the other hand, the values of β_4 and β_6 have no experimental values. For the β_4 value, the calculated value from the finite-range droplet model, FRDM2012 [44], was adopted, and for the β_6 values, the same value as in the previous study [25] was used. Regarding parameters for the coupling of the neutron transfer reaction, the Q value of the one-neutron transfer reaction from ^{248}Cm to ^{51}V was determined based on the mass of the relevant nuclides [47]. The remaining parameters, the potential depth V_0 of the real part of the optical potential and the coupling strength F_{tr} of the neutron transfer reaction, were adjusted to reproduce the present experimental results of the reflection probability $R(E)$.

In Fig. 5, the experimental results were compared to the calculations mentioned above. The single-channel calculation (black dotted line), which considers only the optical potential without any coupling, does not reproduce the experimental trends of $R(E)$ and $D(E)$. The coupled-channels calculation with only the vibrational coupling of the projectile nucleus (green dashed line) also failed to reproduce the experimental values. On the other hand, when the rotational coupling of the deformed target is considered in addition to the above coupled-channels calculation, the calculation (blue dot-dashed line) reproduces the experimental trend well for both $R(E)$ and $D(E)$. Furthermore, by considering the full couplings, where transfer coupling is also added, the agreement is further improved, as shown by the red solid line. Therefore, in the ^{51}V+^{248}Cm system, the effect of the deformation of the target nucleus ^{248}Cm is particularly significant for the QE barrier distribution. This is consistent with the existing QE barrier distribution results for the other hot-fusion reaction systems involving lighter projectile particles [23, 25].

B. Derivation of average Coulomb barrier height B_0

In a hot-fusion reaction system using an actinide target, the experimental results of fusion-fission and QE barrier distribution demonstrate that a compound nucleus is formed more easily when two nuclei collide along the short axis of the prolately deformed target nucleus [25–31, 45, 49], which is called the side collision. In other words, the side collision is favorable to synthesize ERs. Therefore, we derive the energy of the side collision B_{side} for ^{51}V+^{248}Cm from the present experimental data.

First, from the present $R(E)$, we derived the average Coulomb barrier height B_0 [25], which is defined as the energy at $R = 0.5$. By interpolating the $R(E)$ values around $R = 0.5$ at $E_{\mathrm{c.m.}} = 224.9$ and 226.6 MeV, the B_0 value can be obtained as follows:

$$B_0 = 225.6 \pm 0.2 \text{ MeV}. \tag{5}$$

In this case, as illustrated in Fig. 5, $D(E)$ has a maximum value when $E_{\mathrm{c.m.}} = B_0$.

The B_0 values of several reaction systems with the ^{248}Cm target are shown in Fig. 6(b) as a function of the normalized factor, $Z_{\mathrm{P}}Z_{\mathrm{T}}/\left(A_{\mathrm{P}}^{1/3} + A_{\mathrm{T}}^{1/3}\right)$, where $Z_{\mathrm{P,T}}$ and $A_{\mathrm{P,T}}$ represent atomic number and mass number, respectively, and the indexes "P" and "T" indicate projectile and target, respectively. The present result of ^{51}V agrees with the fitting result of the linear function (black line) for the data with lighter projectiles [25, 48]; however, in more detail, the present experimental B_0 value for ^{51}V (Eq. (5)) is 2.7-MeV smaller than the corresponding value of 228.3 ± 1.1 MeV obtained by extrapolating the systematics of lighter-projectile cases, as shown in Fig. 6(a).

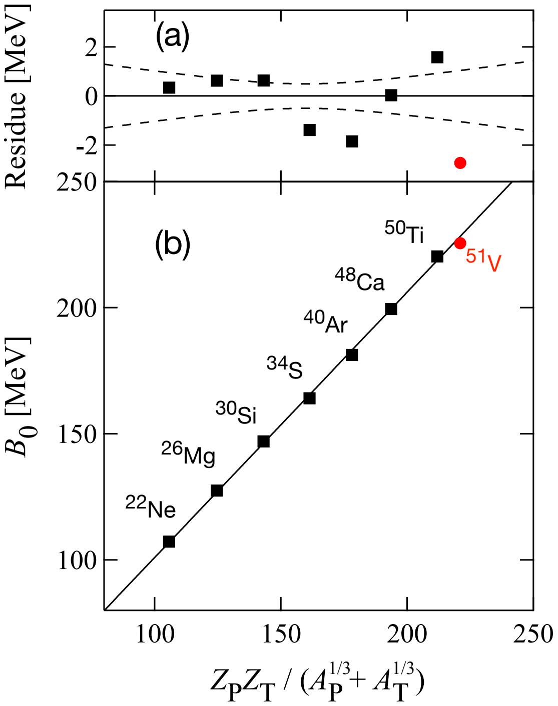

FIG. 6. (a) Residues of the experimental data from the fitting function in panel (b). The dashed lines indicate the uncertainty in the fitting function. (b) Experimental average Coulomb barrier height B_0 of the reaction systems with ^{248}Cm as a function of $Z_P Z_T / \left(A_P^{1/3} + A_T^{1/3}\right)$. The present results of ^{51}V and existing results [25, 48] are represented by red circles and black squares, respectively. The solid line indicates the linear function determined by fitting existing data.

C. Extraction of side-collision energy B_{side}

The side-collision energy B_{side} was obtained by following the same procedure as in Ref. [25]. The theoretical average Coulomb barrier height, $\langle B \rangle$ is defined as

$$\langle B \rangle = \int_0^{\pi/2} B(\theta) \sin\theta d\theta, \tag{6}$$

The orientation-angle dependence of the Coulomb barrier height $B(\theta)$ was calculated using the optical potential $V(r, \theta)$ with the parameters in Table I, except for V_0. The potential depth V_0 was slightly adjusted such that $\langle B \rangle$ coincided with the B_0 value (Eq. (5)). Consequently, the side-collision energy B_{side}, which is equivalent to $B(\theta = 90^\circ)$, is derived as

$$B_{\mathrm{side}} = 233.0 \pm 0.2 \text{ MeV}. \tag{7}$$

Here, the value of B_{side} is 3.3% larger than that of B_0.

In Fig. 7, the derived B_0 (closed arrow) and B_{side} (open arrow) were compared with the QE barrier distribution. From Eq. (4), the components of the barrier distribution corresponding to the side-collision configuration can be extracted [19, 25]. The partial values $r_i(E)$ and $d_i(E)$ for $R(E)$ and $D(E)$, respectively, are defined as

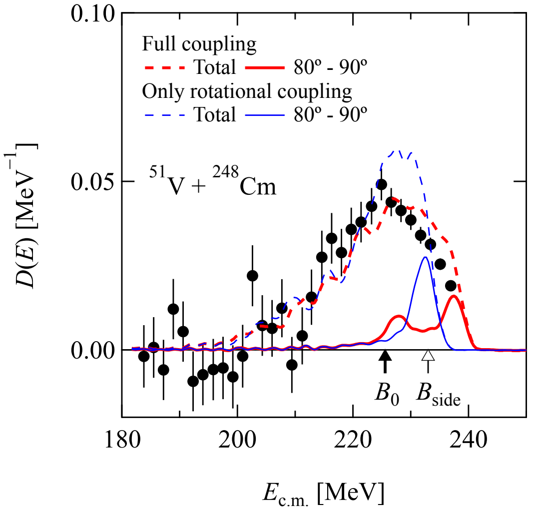

FIG. 7. Present results of quasielastic barrier distribution as a function of $E_{\mathrm{c.m.}}$ with the coupled-channels calculations. The red and blue dashed lines represent the total quasielastic barrier distributions $D(E)$ with full coupling and only the rotational coupling of ^{248}Cm, respectively. The corresponding solid lines indicate the partial barrier distributions between 80° and 90°, $d_{80^\circ - 90^\circ}$. The black closed and open arrows indicate the values of B_0 (Eq. (5)) and B_{side} (Eq. (7)).

$$r_i(E) = \int_{\theta_i^{\min}}^{\theta_i^{\max}} r(E, \theta) \sin\theta d\theta, \tag{8}$$

$$d_i(E) = -\frac{dr_i(E)}{dE}, \tag{9}$$

where subscript "i" denotes the integration interval ($\theta_i^{\min}$–$\theta_i^{\max}$). Figure 7 shows $D(E)$ (red dashed line) by the coupled-channels calculation considering fully couplings and the corresponding side-collision component (orientation angle is 80–90°), $d_{80^\circ - 90^\circ}$ (red solid line). The B_0 is located at a lower energy than a large part of the $d_{80^\circ - 90^\circ}$ distribution, whereas the B_{side} is located near the center of $d_{80^\circ - 90^\circ}$.

To observe the effect of coupling other than the rotational excitation on the side-collision energy, the calculation with only the coupling of the rotation of the deformed target is also shown by the blue lines in Fig. 7. A comparison of these two calculations indicates that the peak of the $d_{80^\circ - 90^\circ}$ distribution splits into two peaks owing to the contributions of the couplings other than the rotational excitation (mainly from the neutron transfer reaction). However, the center of the $d_{80^\circ - 90^\circ}$ distribution did not change significantly and remained close to the B_{side}. Therefore, B_{side} can be regarded as a good quantity for probing the reaction energy for the side-collision configuration.

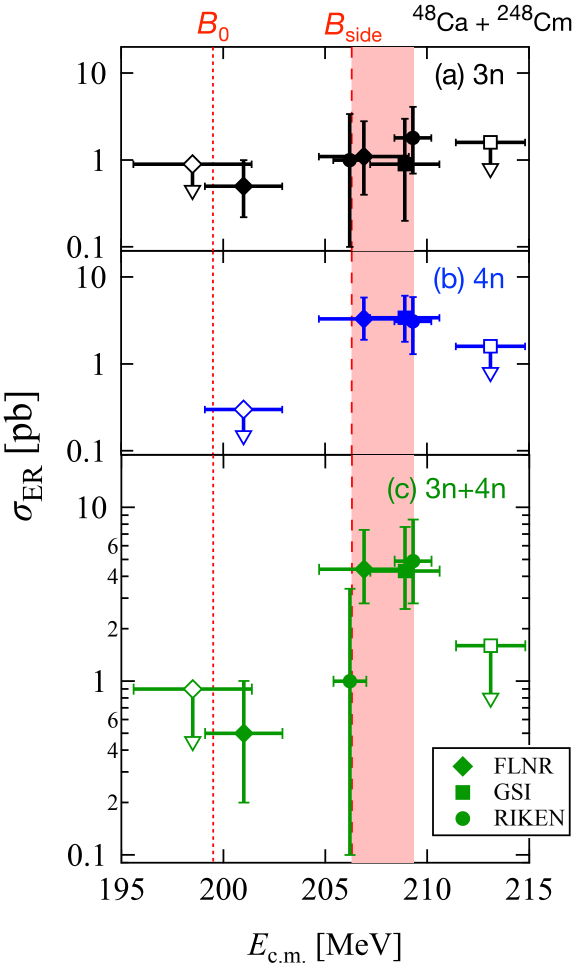

FIG. 8. Experimental excitation functions of evaporation-residue cross sections of (a) 3n, (b) 4n, and (c) 3n+4n channels for the ^{48}Ca+^{248}Cm system measured at FLNR [5, 50], GSI [12], and RIKEN [51]. Open symbols with the triangular arrows indicate the upper-limit values. The horizontal bar indicates the energy change of the target. The red dotted and dashed lines along the vertical axis indicate the B_0 and B_{side} values, respectively, with the B_{side} value corrected by +2 MeV with respect to the previous analysis [25]. The shaded region (+1.5% relative to B_{side}) represents the evaluated uncertainty of the relation between B_{side} and the optimal energy to maximize σ_{ER}.

D. Estimation of optimal energy for evaporation-residue synthesis from ^{51}V+^{248}Cm

From the above discussion, the energy to form a compact system of ^{51}V+^{248}Cm system was estimated. As mentioned in the introduction, a systematic comparison of the QE barrier distribution with the excitation function of σ_{ER} shows that B_{side} is more consistent with the optimal energy E_{opt}, which results in a maximum value of σ_{ER} compared to B_0 in the hot-fusion reaction [25]. However, there is a possibility that the B_{side} and E_{opt} values do not coincide exactly, especially in a system where the product of the atomic numbers of the projectile and target nuclei is large. For example, a theoretical study using the fusion-by-diffusion model suggested that E_{opt} is 2–3 MeV higher than the B_{side} derived from the QE barrier distribution for the ^{48}Ca+^{248}Cm system because of the contribution of the diffusion process following the capture process [49]. On the other hand, as mentioned later in detail in Fig. 9, the theoretical relation between E_{opt} and B_{side} (or B_0) for the ^{51}V+^{248}Cm system also has a large uncertainty [16, 17]. Furthermore, there is no direct experimental information to evaluate the relation between E_{opt} and B_{side} in the ^{51}V+^{248}Cm system. Therefore, we aimed to deduce E_{opt} from the obtained B_{side} value based on the available experimental data for a similar system, to avoid the uncertainty caused by the theoretical calculations as much as possible.

In the following, a possible discrepancy between E_{opt} and B_{side} is investigated in the ^{48}Ca+^{248}Cm system. The ^{48}Ca+^{248}Cm system is the most similar to the ^{51}V+^{248}Cm system among the reaction systems with the same target for which experimental data of both the QE barrier distribution and σ_{ER} are available [5, 12, 25, 50, 51]. Then, we assume that the correspondence between the B_{side} and E_{opt} is the same for both reactions at the ^{248}Cm target, with ^{48}Ca and ^{51}V projectiles. We note that this assumption is not validated yet by the respective excitation function measurement. The relation between E_{opt} and B_{side} can eventually changes for ^{48}Ca and ^{51}V projectiles due to the several effects such as different Coulomb factor and neutron excess, and double-magicity of ^{48}Ca. To clarify this possibility, future experimental and theoretical studies for the ^{51}V+^{248}Cm system itself are strongly desired.

The experimental excitation functions of the σ_{ER} data for the 3n, 4n, and 3n+4n channels for the ^{48}Ca+^{248}Cm system [5, 12, 50, 51] are shown in Fig. 8(a), (b), and (c), respectively, together with the B_0 (dotted line) and B_{side} (dashed line) values determined from the QE barrier distribution measurement for this system [25]. As pointed out in Ref. [25], B_{side} is located around the maximum of σ_{ER} of the 3n+4n channels. However, a more detailed comparison shows that E_{opt} is potentially located in a slightly higher-energy region than B_{side}. Considering the above possibility, in this study, it was assumed that E_{opt} for the ^{48}Ca+^{248}Cm system is located between the B_{side} (206.3 MeV) and 209.3 MeV, as shown by the red-shaded region in Fig. 8. Here, 209.3 MeV is the maximum energy at which a finite value of σ_{ER} was obtained [51]. The width of this uncertainty, denoted by ΔE_{opt}, was 1.5% of B_{side}. Then, assuming a similar situation in the case of the ^{51}V+^{248}Cm system, the E_{opt} that maximizes the σ_{ER} for $^{248}\text{Cm}(^{51}\text{V}, 3\text{–}4\text{n})^{295\text{–}296}119$ was evaluated to be at most 1.5% larger than B_{side} given by Eq. (7):

$$\Delta E_{\text{opt}} = +0.015 \times B_{\text{side}} = +3.5 \text{ MeV}. \qquad (10)$$

Note that the uncertainty ΔE_{opt} is within the broadening of $d_{80^\circ\text{–}90^\circ}$ for full couplings, as shown in Fig. 7.

The obtained values of B_0, B_{side}, and ΔE_{opt} for the

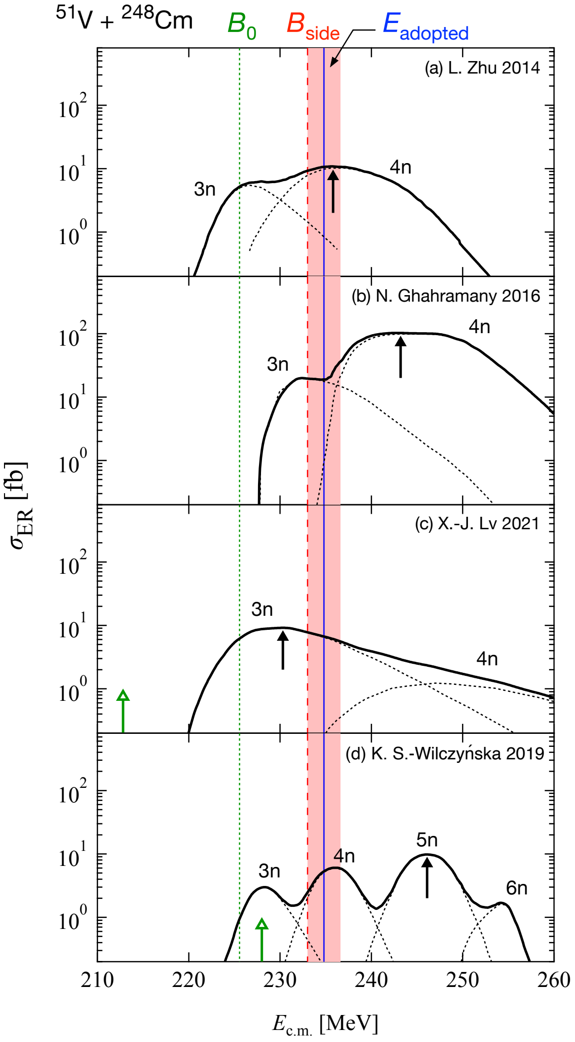

FIG. 9. (a-d) Theoretical calculations of σ_{ER} for ^{248}Cm(^{51}V, xn)$^{299-x}$119 [13, 14, 16, 17]. The black dotted and bold solid lines represent the σ_{ER} of respective channels and their total values, respectively. The black closed arrows indicate the peak energies at which the theoretical σ_{ER} has a maximum value. The green open arrows in plots (c) and (d) indicate the B_0 values used in respective calculations. The green dotted, red dashed, and blue solid lines along the vertical axis indicate the values of B_0 (Eq. (5)), B_{side} (Eq. (7)), and $E_{adopted}$ (Eq. (11)). The red-shaded region indicates the uncertainty of the relation between E_{opt} and B_{side} evaluated from the experimental data of the ^{48}Ca+^{248} Cm system, ΔE_{opt} (Eq. (10)).

^{51}V+^{248}Cm system are compared with the theoretical excitation functions of σ_{ER} in Fig. 9. Black closed arrows in Fig. 9 indicate the energies where the sum of σ_{ER} (black bold lines) has maximum values, i.e., the theoretical optimal energies. The B_0 values used for the calculations by Lv *et al.* (plot (c)) and Siwek-Wilczyńska *et al.* (plot (d)) are also indicated by green open arrows. In these calculations, the barrier distributions were assumed to be a Gaussian function with parameters of the width and mean value (B_0), which were determined from the existing datasets of fusion-fission and fusion-evaporation cross sections of lighter mass systems compared to the ones leading to SHEs [52, 53]. Note that the theoretical B_0 values for the ^{48}Ca+^{248}Cm system of Lv *et al.* and Siwek-Wilczyńska *et al.* are 186 and 201 MeV, respectively, while the experimental value is 199.5 MeV [25]. The deviations of theoretical B_0 values from the experimental ones tend to be similar for the ^{48}Ca and ^{51}V projectiles on ^{248}Cm: approximately +2 MeV and −13 MeV for the calculations by Siwek-Wilczyńska *et al.* and Lv *et al.*. Regarding Fig. 9(a,b), the theoretical B_0 values are not available in Refs. [13, 14].

The theoretical calculations by Zhu *et al.* [13] (Fig. 9(a)) and Adamian *et al.* [15] predicted the optimal energy closer to the B_{side} deduced experimentally, $E_{c.m.} \approx 237$ MeV, where the 4n channel has the largest cross section. The theoretical calculation by Ghahramany *et al.* (Fig. 9(b)) also indicates that the 4n channel has a maximum cross section, but at approximately $E_{c.m.} = 243$ MeV [14]. On the other hand, the calculation by Lv *et al.* [17] (Fig. 9(c)) predicts the maximum cross section at the 3n channels. Although the calculation by Siwek-Wilczyńska *et al.* [16] (Fig. 9(d)) predicts the maximum cross section at the 5n channels, the theoretical optimal energy for the 4n channel by Siwek-Wilczyńska *et al.*, $E_{c.m.} \approx 236$ MeV, was close to the B_{side} value. In addition, Figure 9 also shows clearly that the shape of the theoretical excitation function strongly depends on the theory adopted. Thus, the theoretical calculations predict significantly different excitation functions with each other in terms of the shape, optimal reaction energy, and channel having a maximum cross section. These differences potentially result from a different treatment of the processes of compound-nucleus formation and its deexcitation following the capture process in each theory. Therefore, to avoid this theoretical uncertainty, the present estimation of the optimal reaction energy was performed based only on the experimental information with the assumption of the similarity between the projectiles of ^{48}Ca and ^{51}V for the reactions involving ^{248}Cm targets. Future theoretical investigation considering the present experimental B_0 value would be interesting to obtain a more reliable optimal reaction energy.

Finally, considering the B_{side} experimentally obtained by the QE barrier distribution measurement and the corresponding uncertainty ΔE_{opt}, one possibility is to choose the central value of the shaded region, as shown by the blue solid line in Fig. 9 as the adopted energy, $E_{adopted}$ for the synthesis of element 119 via the ^{51}V+^{248}Cm reaction:

$$E_{adopted} = B_{side} + \frac{1}{2} \times \Delta E_{opt} = 234.8 \text{ MeV}. \qquad (11)$$

Assuming a target of 500-μg/cm^2-thick Cm$_2$O$_3$, the energy change in the target is ±1.9 MeV relative to $E_{adopted}$. Thus, the spread of the reaction energy,

$\Delta E_{\rm opt}/2 = 1.8$ MeV, covers the difference between the $B_{\rm side}$ and $E_{\rm adopted}$. The obtained reaction energy of 234.8 ± 1.8 MeV corresponds to an excitation energy of 40.3 ± 1.8 MeV for the compound nucleus $^{299}119^*$, using the experimental mass excesses of projectile and target nuclei [54] and the theoretical value from Ref. [55], respectively.

IV. SUMMARY

We measured the excitation function of the quasielastic (QE) backscattering cross sections relative to the Rutherford cross sections in the ^{51}V+^{248}Cm system at the SRILAC facility, RIKEN, and extracted the QE barrier distribution. The backscattering events were measured by detecting the target-like nuclei recoiled at 0° using GARIS-III. Coupled-channels calculations were performed to understand the reaction dynamics of the ^{51}V+^{248}Cm system. A comparison of the calculations with the experimental data indicated that the rotational excitation of the deformed target nucleus ^{248}Cm significantly affected the QE barrier distribution, which is similar to that of other hot-fusion-reaction systems. The average Coulomb barrier height B_0 for ^{51}V+^{248}Cm was derived from the present experimental data. The present B_0 value for ^{51}V+^{248}Cm was roughly consistent with the systematics of the experimental B_0 values in other reaction systems with a ^{248}Cm target, even though the present value was slightly smaller. The energy for side collision $B_{\rm side}$, with which the colliding nuclei form a spatially compact system, was extracted from the experimental data by considering the deformation of ^{248}Cm. The relation between $B_{\rm side}$ and the optimal reaction energy for maximizing $\sigma_{\rm ER}$ was evaluated in the ^{48}Ca+^{248}Cm system. From the $B_{\rm side}$ value for ^{51}V+^{248}Cm obtained in the present work and the relation between the $B_{\rm side}$ and $E_{\rm opt}$ evaluated in the ^{48}Ca+^{248}Cm system, the optimal reaction energy for the synthesis of element 119 from the ^{248}Cm(^{51}V, 3–4n)$^{295-296}$119 reaction was estimated to be 234.8 ± 1.8 MeV with an aid of presented experimental data.

ACKNOWLEDGMENTS

We would like to express our gratitude to the accelerator staff at RIKEN Nishina Center for providing ^{51}V beam under the extremely stable operation and performing the quick change of the supplied beam energy during the entire machine time. The ^{248}Cm isotope used in this research was supplied by the U.S. Department of Energy Isotope Program, managed by the Office of Isotope R&D and Production. The authors would like to thank Dr. T. Tanaka for the fruitful discussions on the interpretation of the data. The present work was supported in part by Grant-in-Aid for JSPS Research Fellow Grant No. 20J01229 and for JSPS KAKENHI Grant No. 20H01918. This work was partially supported by the U.S. DOE under the Contract No. DE-AC05-00OR22725.

[1] W.D. Myers and W.J. Swiatecki, Nucl. Phys. **81**, 1 (1966).
[2] Yu. Ts. Oganessian *et al.*, Phys. Rev. C **63**, 011301 (2000).
[3] Yu. Ts. Oganessian *et al.*, Phys. Rev. C **69**, 021601(R) (2004).
[4] Yu. Ts. Oganessian *et al.*, Phys. Rev. C **69**, 054607 (2004).
[5] Yu. Ts. Oganessian *et al.*, Phys. Rev. C **70**, 064609 (2004).
[6] Yu. Ts. Oganessian *et al.*, Phys. Rev. C **74**, 044602 (2004).
[7] Yu. Ts. Oganessian *et al.*, Phys. Rev. Lett. **104**, 142502 (2010).
[8] Yu. Ts. Oganessian *et al.*, Phys. Rev. C **79**, 024603 (2009).
[9] S. Hofmann *et al.*, GSI Report **2008**, 131 (2009).
[10] S. Hofmann *et al.*, Eur. Phys. J. A **52**, 180 (2016).
[11] J. Khuyagbaatar *et al.*, Phys. Phys. C **102**, 064602 (2020).
[12] S. Hofmann *et al.*, Eur. Phys. J. A **48**, 62 (2012).
[13] L. Zhu, W.J. Xie, and F.-S. Zhang, Phys. Rev. C **89**, 024615 (2014).
[14] N. Ghahramany and A. Ansari, Eur. Phys. J. A **52**, 287 (2016).
[15] G.G. Adamian, N.V. Antonenko, and H. Lenske, Nucl. Phys. A **970**, 22 (2018).
[16] K. Siwek-Wilczyńska, T. Cap, and M. Kowal, Phys. Rev. C **99**, 054603 (2019).
[17] X.-J. Lv, Z.-Y. Yue, W.-J. Zhao, and B. Wang, Phys. Rev. C **103**, 064616 (2021), and private communication.
[18] H. Timmers *et al.*, Nucl. Phys. A **584**, 190 (1995).
[19] K. Hagino and N. Rowley, Phys. Rev. C **69**, 054610 (2004).
[20] S. Mitsuoka *et al.*, Phys. Rev. Lett. **99**, 182701 (2007).
[21] S.S. Ntshangase *et al.*, Phys. Lett. B **651**, 27 (2007).
[22] G. Kaur *et al.*, Acta Phys. Pol. **49**, 651 (2018).
[23] T. Tanaka *et al.*, J. Phys. Soc. Jpn. **87**, 014201 (2018).
[24] T. Niwase *et al.*, JPS Conf. Proc. **32**, 010022 (2020).
[25] T. Tanaka *et al.*, Phys. Rev. Lett. **124**, 052502 (2020), and private communication.
[26] D. J. Hinde *et al.*, Phys. Rev. Lett. **74**, 1295 (1995).
[27] D. J. Hinde *et al.*, Phys. Rev. C **53**, 1290 (1996).
[28] K. Nishio *et al.*, Phys. Rev. C **62**, 014602 (2000).
[29] A. Narisov *et al.*, Nucl. Phys. A **759**, 342 (2005).
[30] K. Nishio *et al.*, Phys. Rev. C **77**, 064607 (2008).
[31] D. J. Hinde *et al.*, Phys. Rev. C **97**, 024616 (2018).
[32] RIKEN Accel. Prog. Rep. **54**, S1 (2021).
[33] T. Watanabe *et al.*, Proc. of the 14th Ann. Meeting of Part. Acc. Soc. of Jpn, WEP091 (2017).

[34] D. Kaji *et al.*, Nucl. Instrum. Methods Phys. Res. B **317**, 311 (2013).

[35] S. Ishizawa *et al.*, Nucl. Instrum. Methods Phys. Res. A **960**, 163614 (2020).

[36] S. B. Kaufman *et al.*, Nucl. Instrum. Methods **5**, 47 (1974).

[37] K. Hagino, N. Rowley, and A. T. Kruppa, Comput. Phys. Commun. **123** 143 (1999).

[38] O. Akyüz and A. Winther, in *Proceedings of the International School of Physics "Enrico Fermi," Course LXXVII, Varenna, 1979*, edited by R. A. Brogila, C. H. Dasso, and R. A. Rocci (North-Holland, Amsterdam, 1981), p. 492.

[39] W. Jimin and H. Xiaolong, Nucl. Data Sheets **144**, 1 (2017).

[40] G. Colucci *et al.*, Eur. Phys. J. A **55**, 111 (2019).

[41] K. Hagino and N. Takigawa, Prog. of Theo. Phys. **128** (2012) 1061.

[42] K. Hagino, K. Ogata, and A.M. Moro, arXiv:2201.09512.

[43] B. Pritychenko *et al.*, Atom. Data and Nucl. Data Tables **107**, 1 (2016).

[44] P. Möller, A.J. Sierk, T. Ichikawa, and H. Sagawa, Atom. Data and Nucl. Data Tables **109–110**, 1 (2016).

[45] K. Hagino and T. Tanaka, JPS Conf. Proc. **32**, 010020 (2020).

[46] M. J. Martin, Nucl. Data Sheets **122**, 377 (2014).

[47] M. Wang *et al.*, Chin. Phys. C **45**, 030003 (2021).

[48] T. Tanaka, Doctoral dissertation, Kyushu University, 2019, `https://catalog.lib.kyushu-u.ac.jp/opac_download_md/2236025/sci1328.pdf`.

[49] K. Hagino, Phys. Rev. C **98**, 014607 (2018).

[50] Yu. Ts. Oganessian *et al.*, Phys. Rev. C **63**, 011301(R) (2001).

[51] D. Kaji *et al.*, J. Phys. Soc. Jpn. **86**, 034201 (2017).

[52] K. Siwek-Wilczyńska and J. Wilczyński, Phys. Rev. C **69**, 024611 (2004).

[53] B. Wang *et al.*, Atom. Data and Nucl. Data Tables **114**, 281 (2017).

[54] M. Wang, W.J. Huang, F.G. Kondev, G. Audi, and S. Naimi, Chin. Phys. C **45**, 030003 (2021).

[55] W.D. Myers and W.J. Swiatecki, Nucl. Phys. A **601**, 141 (1996).